Journal of Environmental Chemical Engineering 11 (2023) 110755

Contents lists available at ScienceDirect

Journal of Environmental Chemical Engineering

journal homepage: www.elsevier.com/locate/jece

Mineralization of polystyrene nanoplastics in water by photo-Fenton oxidation

Carla di Luca [a,b,*], Jorge Garcia [a], David Ortiz [a], Macarena Munoz [a,**], Jaime Carbajo [c], Zahara M. de Pedro [a], Jose A. Casas [a]

[a] Departamento de Ingeniería Química, Universidad Autónoma de Madrid, Ctra. Colmenar km 15, 28049 Madrid, Spain
[b] División Catalizadores y Superficies, Instituto de Investigaciones en Ciencia y Tecnología de Materiales (INTEMA-CONICET), Av. Colón 10850, 7600 Mar del Plata, Argentina
[c] Departamento de Ingeniería Química, Universidad Complutense de Madrid, Avda. Complutense s/n, 28040 Madrid, Spain

ARTICLE INFO

Editor: Despo Kassinos

Keywords:
Photo-Fenton
Polystyrene
Nanoplastics
Advanced oxidation processes
Water treatment

ABSTRACT

Wastewater treatment plants (WWTPs) have been identified as hotspots for the spread of micro(nano)plastics (MPs/NPs) in water. Advanced oxidation processes (AOPs) have emerged as promising alternatives for tackling MPs/NPs pollution, however, the number of studies on this topic remains quite limited and needs further research. In this study, the feasibility of the photo-Fenton process (UV/ H_2O_2/ Fe^{3+}) carried out at ambient conditions and using a broad-spectrum UV-Vis lamp was investigated for the degradation of polystyrene (PS) NPs in water. The impact of the main variables of the process, namely initial PS concentration, Fe^{3+} concentration, initial pH, H_2O_2 dose and particle size, was evaluated. Under optimized operating conditions ($[PS\ NPs]_0 = 20$ mg L^{-1}; $[Fe^{3+}]_0 = 1$ mg L^{-1}; $[H_2O_2]_0 = 130$ mg L^{-1}; $pH_0 = 3$ and T = 25 ºC), complete mineralization of PS NPs (140 nm) was achieved in 40 min. The outstanding performance of the process was mainly due to the wavelength and light intensity of the UV-lamp employed. To the best of our knowledge, this is the first study in the field of photoassisted AOPs reporting the complete and fast mineralization of PS NPs in water, under ambient conditions. According to our results, photo-Fenton process can be applied to higher loads and larger particle sizes by adjusting the supplied oxidant dose and extending the reaction time. Hence, the photo-Fenton process displays great potential for producing high-quality reclaimed water and/or to be combined with a conventional separation process to treat concentrate streams and mineralize NPs at WWTPs.

1. Introduction

The outstanding properties of plastics have made these materials omnipresent in the world around us. Routinely used in simple daily requirements, plastics have improved substantially our life quality and are considered a pillar material in a global "throwaway culture" economy. In 2021, global plastic production reached almost 390 million tons [1], and it is expected to double in the next 20 years [2]. The dark side of this flourishing story is the generation and poor management of plastic wastes. Depending on their use, the service life of plastic products can vary from 1 day to over 50 years before being disposed as plastic waste where it is used for energy recovery (12%), recycled (9%), discarded in landfill (8%) or lost to the environment (71%) [3]. This situation poses a tremendous burden on the worldwide ecosystems as these materials are hardly degradable and can persist for years to decades, or even centuries [4].

Microplastics (MPs), defined as plastic particles smaller than 5 mm, are the most extended plastic debris in the environment [5]. Recent classifications have also distinguished nanoplastics (NPs), particles smaller than < 1 μm that can be either emitted to or formed in the environment [6,7]. NPs have been less investigated but are potentially the most hazardous as they are more likely to pass biological membranes and thus, to affect the functioning of cells [8]. While further information on the impacts of MPs/NPs on the aquatic life and human health is emerging, indications are that these tiny particles present a risk as a result of physical blockages, tissue toxicity, inherent contaminants leaching, and chemical/biological exposures from contaminants/bacteria adsorbed onto plastic particles given their high

* Corresponding author at: Departamento de Ingeniería Química, Universidad Autónoma de Madrid, Ctra. Colmenar km 15, 28049 Madrid, Spain.
** Corresponding author.
E-mail addresses: carla.diluca@uam.es (C. di Luca), macarena.munnoz@uam.es (M. Munoz).

https://doi.org/10.1016/j.jece.2023.110755
Received 3 May 2023; Received in revised form 9 August 2023; Accepted 11 August 2023
Available online 16 August 2023
2213-3437/© 2023 The Author(s). Published by Elsevier Ltd. This is an open access article under the CC BY-NC-ND license (http://creativecommons.org/licenses/by-nc-nd/4.0/).

exposed surface area [9–11].

Water is considered the main vector for the spread of MPs/NPs and municipal Wastewater Treatment Plants (WWTPs) are recognized as a significant hotspot of this kind of contamination [6,7,11–13]. Although WWTPs can achieve MPs removal efficiencies above 90%, they still represent the major source of these particles in the aquatic environment given the huge volume continuously discharged by these facilities. Furthermore, an evident decrease of MPs particle size upon WWTP treatments has been found which, apart from the easier removal of large particle sizes, can be due to MPs fragmentation [13]. In a recent comprehensive review, it was demonstrated that while particles above 1000 μm constitute 80 – 95% of the influent MPs, this fraction represented less than 8% in secondary effluents [6].

In this context, the development of advanced water treatment technologies to prevent the emission of low-size MPs and NPs from WWTPs is urgently required. Advanced oxidation processes (AOPs) have emerged as promising water treatment technologies for the elimination of different emerging pollutants such as pharmaceuticals, personal care products, pesticides or hormones [14,15]. In brief, AOPs rely on the in-situ generation of oxidative radicals with different values of standard reduction potential, such as the hydroxyl radical (HO•). Once these radicals are formed, a cascade of mechanistically complex reactions occur. These radicals are non-selective oxidants and can transform complex organic compounds into simpler ones or even mineralize them to CO_2 and H_2O [16]. Among its advantages, these processes provide rapid reaction rates and have the benefit of oxidizing organic pollutants rather than transferring or concentrating them into a new waste stream such as solid waste by filtration [17]. Nevertheless, unlike other processes that are more mature for the removal of MPs/NPs (e.g. filtration technologies), the application of AOPs for MPs/NPs degradation has been scarcely investigated as denoted by the publication date (2019 – 2023) of the main literature in the field, and the reported results suggested that MPs/NPs degradation by AOPs remains a challenge to the scientific community [16,18–21].

Table 1 summarizes the literature works dealing with the application of AOPs for MPs/NPs removal from water. Photocatalysis has received major attention, but results are still far from being promising. After considerably high reaction times (up to 7 days), the oxidation of LDPE microfilms of 50 μm thickness by photocatalysis with ZnO-based nanocomposites only led to the generation of cracks and spots at the surface of the particles as well as the formation of superficial oxygenated groups, which increased the carbonyl and vinyl indexes [22,23]. Razali, et al. reached enhanced oxidation yields of PP microparticles operating at 50 ºC and using the same kind of catalyst, but less than 10% of mass loss was found at the end of the reaction (6 h) [24]. More recently, Domínguez-Jaimes, et al. used different TiO_2 structures for the photocatalytic oxidation of PS NPs at ambient temperature, obtaining up to 13% mineralization after 50 h reaction time [25]. Similar results have also been reported by the recent works of Allé et al. and Acuña-Bedoya et al., where at the most 50% mineralization of PS NPs was achieved [26, 27]. The use of activated persulfate for MPs removal (PE, 0.01 −1.5 mm) has also been addressed in a recent work [28], but extremely severe operating conditions (160 ºC, 6.5 mM peroxymonosulfate) were required to achieve 54% mass loss after 8 h reaction time. Other two photoassisted processes, such as UV/ peroxymonosulfate and UV/H_2O_2, were recently evaluated for the degradation of PS NPs and PET microfibers, respectively, achieving interesting levels of mineralization (c.a. 64% for PS NPs) and mass loss (up to 21.6% for PET fibers) [17,29].

Despite its cost-effectiveness, the Fenton process has been scarcely studied for MPs/NPs oxidation so far. In our recent contribution, up to 70% mineralization of monodispersed PS NPs spiked in deionized water was achieved, but at the expense of severe operating conditions (80ºC) and high reagents consumption [35]. Our hypothesis maintained that the oxidation process starts in MPs/NPs surface, leading to the formation of oxygen functional groups, which consequently increase their acidity and hydrophilicity and progressively reduce their size, ultimately resulting in their complete oxidation to CO_2. The intensification of this technology may significantly enhance both the kinetics and mineralization yield. Recently, Miao, et al. investigated the degradation of PVC MPs via an electro-Fenton-like system with a TiO_2/graphite cathode [34]. Mass losses above 50% were achieved after 6 h reaction time, but again, severe operating conditions were required ($T_{cathode} = 100$ ºC). In a pioneering work, Feng et al. explored the photoassisted Fenton degradation of PS MPs, achieving up to 89% of mineralization of sulfonated cross-linked PS beads [33]. The sulfonate decorations increased the hydrophilicity of MPs' surface and provided cation-exchange properties, which were useful to anchor Fe species and boost MPs' oxidation. However, virgin PS microspheres (without sulfonation pretreatment) did not show significant changes after the applied treatment. In a recent contribution, Marcelino-Perez et al. studied the photo-Fenton oxidation of polyamide 66 microfibers using solar and LED irradiation [32]. Under the conditions considered, only surface defects and an increase in the specific surface area were registered. Likewise, Piazza et al. examined the heterogeneous photo-Fenton of PP and PVC MPs using systems based on ZnO/SnO_2/Fe^0 irradiated in the visible spectrum [31]. After one week, a reduction of 95% in particle volume and the formation of new functional groups were obtained. In this context, the application of photo-Fenton process has displayed great potential for future applications, but it has been only incipiently considered, and more in-depth research and optimization are required [20].

The aim of this study was to investigate the degradation of polystyrene nanoplastics in water using an homogeneous Fenton process intensified with broad-spectrum irradiation, ranging from UVC to visible light, for the first time. For this, a screening of UV-based technologies for the removal of PS NPs was firstly investigated (UV, UV/Fe^{3+},UV/H_2O_2 and photo-Fenton (UV/H_2O_2/Fe^{3+}) and contrasted to the classic Fenton process (H_2O_2/ Fe^{3+}). The fate of PS NPs upon photo-Fenton oxidation was then deeply evaluated, considering not only the mineralization yield but also the particle size evolution and turbidity of the reaction medium. A complete operating conditions study was carried out to analyze the impact of initial NPs load, catalyst concentration, initial pH and initial H_2O_2 dose on PS NPs (140 nm) mineralization. Finally, the influence of the particle size (140 and 909 nm) on the performance of the process was investigated under optimized operating conditions.

2. Materials and methods

2.1. Materials and chemicals

Two commercial NPs samples of monodisperse PS, PS-R-KM248 (140 ± 5 nm, 5% w/v), and PS-R-KM123 (909 ± 27 nm, 5% w/v), were purchased from microParticles GmbH. These PS nanoparticles are prepared via free radical-initiated polymerization techniques, obtaining spherical particles with high mechanical and chemical stability, as well as low density (1.05 g/cm^3). The main properties of the commercial PS NPs, together with the oxidation stoichiometry, are provided in Table 2. Nitric acid (65%), titanium (IV) oxysulfate (99%), iron (III) nitrate nonahydrate (98%), and iron (II) sulfate heptahydrate (≥ 99%) were provided by Sigma-Aldrich. Hydrogen peroxide solution (33% w/w) and 2-propanol (IPA) were supplied by Panreac. All these compounds were used as received without further purification. Deionized water was used to perform the oxidation experiments.

2.2. Typical reaction procedure

The experimental set-up used in this work was similar to the one reported in a previous contribution [39]. In brief, oxidation tests were carried out in an immersion-wall batch jacketed photoreactor (0.7 L) equipped with a 150 W medium pressure Hg lamp (Nova Light TQ-150 from Peschl Ultraviolet) confined in a water-cooled quartz chamber provided with a temperature control unit (Ministat 125, Huber). The lamp emits in a broad spectrum between 250 and 600 nm with a

Table 1
Overview of the application of advanced oxidation processes for the treatment of MPs/NPs in water.

AOP	MPs/NPs nature and size	Catalyst	Operating conditions	Analytical methods	Results	Reference
Photocatalysis	LDPE film (50 μm thickness)	ZnO nanorod	50 W dichroic halogen lamp Visible light (≈ 60–70 klux) Petri dish reactor C_{cont} = 1 film of size 1 × 1 cm, C_{cat} = Not provided Ambient temperature Reaction matrix: deionized water	- SEM - Dynamic mechanical analyser - FTIR	After 175 h reaction time: - Cracks and spots - Increased stiffness - New functional groups: carbonyl, hydroperoxide, peroxides and unsaturated groups - 115% increase in carbonyl and vinyl indexes	[22]
	LDPE film (50 μm thickness)	ZnO-Pt nanocomposite	50 W dichroic halogen lamp Visible light (≈ 60–70 klux) Petri dish reactor C_{cont} = 1 film of size 1 × 1 cm C_{cat} = Not provided (ZnO-Pt substrates of 2.5–0.75 cm) Ambient temperature Reaction matrix: deionized water	- SEM-EDX - FTIR	After 175 h reaction time: - Wrinkles, cracks and cavities - New functional groups: carbonyl, hydroperoxide, peroxides and unsaturated groups - 110% and 165% increase in carbonyl and vinyl indexes, respectively	[23]
	PP (25 mm^2 and 100 mm^2)	ZnO nanoparticles	11 W UV lamp UV-C radiation Batch- slurry photoreactor. C_{cont} = 0.025 – 0.1 mm^2/m^2 C_{cat} = 1 – 3 g L^{-1} T = 35 – 50 °C Reaction matrix: deionized water	- Mass loss analysis - SEM - FTIR	After 6 h reaction time: - Microcracks, cavities and interconnected holes - Mass loss = 7.4% (50 °C, 1 g L^{-1} ZnO and 25 mm^2 PP) - New functional groups: carboxyl, alcohol, hydroxyl, ketone	[24]
	PS (315 nm)	TiO_2 structures (barrier, nanotubular and mixed)	UV lamp Pyrex reactor C_{cont} = 9 g L^{-1} C_{cat} = 1 cm^2 of exposed photocatalyst area T = 30 °C Reaction matrix: deionized water	- Turbidimetry - TOC - FTIR - GC/MS	After 50 h reaction time: - Turbidity reduction = 16.2%, 19.7% and 23.5% for TiO_2-B, TiO_2-T and TiO_2-M, respectively (photolysis = 16.1%) - Mineralization = 1.7%, 6.6% and 12.7% for TiO_2-B, TiO_2-T and TiO_2-M, respectively (photolysis = 1.7%) - Carbonyl index = 0.2624, 0.2663 and 0.2755 for TiO_2-B, TiO_2-T and TiO_2-M, respectively (photolysis = 0.2616; fresh NPs = 0.0882)	[25]
	PMMA (105 nm) PS (140 and 508 nm)	TiO_2–P25 on silicon carbide foam	15 W UV-A lamps Tubular quartz reactor with recirculation C_{cont} = 12 mg L^{-1} (TOC) C_{cat} = 55 g L^{-1} Flow rate = 10 – 50 mL min^{-1} Ambient temperature Reaction matrix: distilled water	- TOC	After 7 h reaction time: - Mineralization = 50%, 29% and 15% for PMMA, PS-140 and PS-508, respectively (photolysis PMMA = 8.4%)	[26]
	PS (350 nm)	Cu_2O/CuO	50 W LED lamp Visible spectrum (400–800 nm) Stirred batch reactor C_{cont} = 9 g L^{-1} C_{cat} = 2.6 cm^2 of exposed photocatalyst area T = 30 °C pH = 11–12 Reaction matrix: distilled water	- Turbidimetry - TOC - ATR/FTIR - GC/MS	After 50 h reaction time: - Turbidity reduction = 23.5% (photolysis = 4.1%) - Mineralization = 15%, (photolysis = 0%) - Carbonyl index = 59.75, (photolysis = 9.66; fresh NPs = 0.7) - Six intermediates identified by GC/MS	[27]
	HDPE (200–250 μm) Nylon microspheres (2.38 mm) POM (polyoxomethylene,	BiOCl-X	250 W Xe lamp Visible spectrum (>420 nm) Stirred batch reactor	- Mass loss analysis - FTIR - SEM - Toxicity (zebrafish)	After 5 h reaction time: - Mass loss = 5.4% (HDPE) - Catalyst adsorption onto microplastics	[30]

(*continued on next page*)

Table 1 (*continued*)

AOP	MPs/NPs nature and size	Catalyst	Operating conditions	Analytical methods	Results	Reference
	3 mm) PP red (2.6 mm) PP black (5 mm)		C_{cont} = 1 g L^{-1} (μm plastics) 10 g L^{-1} (mm plastics) C_{cat} = 1 g L^{-1} Ambient temperature Reaction matrix: deionized water		- Particles fragmentation and size reduction - Smoothness reduction - New functional groups: carbonyl, hydroxyl - The decrease in MP size led to an increase of the oxidation rate - Light colors reduce photocatalytic degradation - No significant impact on survival rate and hatching rate of zebra fish of aqueous solution from degraded MPs	
UV/H_2O_2	PET fibers (40 μm x 3 cm)	–	55 W and 11 W fluorescent lamp (254 nm) Stirred batch reactor C_{cont} = 16.7 mg L^{-1} C_{H2O2}= 500 – 2000 mg L^{-1} (every 60 min) T = 18 °C Reaction matrix: deionized water and laundry wastewater	- Mass loss - SEM - AFM - FTIR	After 9 h reaction time: - Mass loss = 21.6% (photolysis = 6%) - Pitting and cracks formation - Increase of CI	[17]
Photo-Fenton	PP (155 μm) PVC (73 μm)	ZnO NRs/ SnO_2/ Fe^0	120 W tungsten-halogen lamp Visible spectrum C_{cont} = 20 mg L^{-1} C_{cat} = not provided C_{H2O2}= 35 mM Flow rate = 300 mL min^{-1} Ambient temperature Reaction matrix: deionized water	- Optical microscope -Particle size analysis - SEM-EDX - FTIR -Ecotoxicity bioassays (Vibrio fischeri, P. subcapitata and D. magna)	After 7 days reaction time: - Reduction of 95% of particle volume - Formation of functional groups (C=O, O–H) - Nontoxic by-products	[31]
	PA6.6 (0.02 –0.2 mm)	$FeCl_3$·6 H_2O	Simulated solar irradiation and natural solar + LED irradiation Stirred batch reactor C_{cont} = 20 mg L^{-1} C_{cat} = 5 mg L^{-1} C_{H2O2}= 10 mg L^{-1} pH 2.8 Ambient temperature Reaction matrix: deionized water	- FESEM - FTIR - DSC - N_2 Physisorption	After 7 h reaction time: - Holes and detachment of surface layers - Functional groups remained unchanged - Fe precipitates on fibers - Increase in surface area due to the appearance of surface defects	[32]
	CS-PS (250 – 350 μm)	$FeCl_3$	250 W Hg (Xe) lamp Broad-band UV C_{cont} = 10,000 mg L^{-1} C_{cat} = 0.42 mM C_{H2O2}= 141 mM pH = 2 Ambient temperature Reaction matrix: deionized water	- SEM - TOC - Mass loss analysis - FTIR - MS Q-TOF	After 300 min: - Smoothness and size reduction - Mineralization > 89% - Binding of Fe(III)/Fe(II) to sulfonated PS is crucial - Mineralization depends on cross-linking degree	[33]
Electro-Fenton-like	PVC (100 –200 μm)	TiO_2/graphite cathode	Applied potential – 0.7 V vs. Ag/AgCl C_{cont} = 100 mg L^{-1} C_{cat} = 0.4 g L^{-1} Oxygen flow = 40 mL min^{-1} T (cathode) = 100 °C pH_0 = 3 Reaction matrix: deionized water (0.05 M Na_2SO_4)	- Mass loss analysis - FTIR -TOC - GC/MS - HPLC - XPS - SEM	After 6 h reaction time: - Smoothness reduction - Mass loss = 56% - Dechlorination = 75% - Generation of functional groups (C=O, O–H) - Six intermediates identified by GC/MS - Short-chain organic acids identified by HPLC as final products - Increase of surface O/C ratio	[34]
Fenton oxidation	PET (150–250 μm) PE (150–250 μm) PVC (150–250 μm) PP (150–250 μm) EPS (20–50 μm; 50 –100 μm; 100 –150 μm; 150–250 μm; 250–500 μm) PS (140 nm)	$Fe(NO_3)_3$·9 H_2O	C_{cont} = 1.3 g L^{-1} (MPs); 20 mg L^{-1} (PS, NPs 140 nm) C_{H2O2}= 1000 mg L^{-1} (MPs); 130 mg L^{-1} (PS, NPs 140 nm) (15 doses) C_{cat} (Fe^{3+}) = 10 mg L^{-1}	- Mass loss analysis - TOC - SEM - TEM - DLS - Elemental analysis - Water contact angle	After 7.5 h reaction time: -Oxidation yield increased for smaller particles -Introduction of oxygenated groups - ↑ acidity and hydrophilicity - 70% mineralization for PS NPs - New absorption bands of C–O,	[35]

(*continued on next page*)

Table 1 (*continued*)

AOP	MPs/NPs nature and size	Catalyst	Operating conditions	Analytical methods	Results	Reference
			(5 doses) $pH_0 = 3$ T = 80 °C Reaction matrix: deionized water	- pH_{slurry} - FTIR	C=O, and O–C=O bonds - Formation of wrinkles, voids and holes at surface	
Fenton oxidation + hydrothermal condition	HDPE (< 100 μm) LDPE (< 100 μm) PS (< 100 μm) PP (< 100 μm) PET (< 100 μm) PVC (< 100 μm)	$FeSO_4 \cdot 7\ H_2O$	$C_{cont} = 0.5 – 2$ g L^{-1} C_{H2O2}= 50 – 500 mM $C_{cat} = 1 – 10$ mM pH = 0.7 – 3 T = 25 – 160 °C Reaction matrix: deionized water, tap water, river water and seawater	- Mass loss analysis - TOC - Raman - XRD - SEM - TGA-DSC - XPS - DLS - Toxicity (*E. coli*)	After 16 h reaction time: - Mass loss at 140 °C= 70% (HDPE), 95% (LDPE), 3% (PVC), PS (96%), PP (90%) and PET (35%). - Lower melting points ensured higher weight losses - mineralization 75.6% (UHMWPE) - Formation of carbonyl groups - ↓ crystallinity - Formation of aggregates, holes and cavities - ↑ hydrophilicity - Nontoxic intermediates - No inhibitory effects in natural water	[36]
UV/PMS	PS (80 nm)	–	6 W low-pressure mercury UV lamp (254 nm) Stirred batch reactor $C_{cont} = 5 – 30$ mg L^{-1} $C_{peroxymonosulfate} = 1.25 – 5$ Mm pH = 3 – 11 T = 25 °C Reaction matrix: deionized water	- Turbidity - TOC - SEM - HPLC-MS - Toxicity	After 6 h reaction time: - 94.3% turbidity removal (photolysis = 21%) - Mineralization = 63.9% (photolysis = 2%) - 14 intermediates identified - Particles decreased in size until disappear	[29]
Heat-activated persulfate	PE (0.01 –1.5 mm)	Mn@NCNTs	$C_{cont} = 5$ g L^{-1} $C_{cat} = 0.2$ g L^{-1} $C_{peroxymonosulfate} = 6.5$ mM T = 100 – 160 °C Reaction matrix: deionized water	- Mass loss analysis - HPLC - TOC - Toxicity (*C. vulgaris*) - GC-MS	After 8 h reaction time: - Mass loss = 54% (160 °C), 45% (140 °C), 40% (120 °C), 8% (100 °C) - Non-toxic intermediates	[28]
Peroxonation (O_3/H_2O_2)	PE (20 mesh)	–	$C_{cont} = 2.5$ g L^{-1} C_{H2O2}= not provided O_3 flow rate = 1 – 5 L min^{-1} pH = 12	- FTIR	After 3 h reaction time: - New functional groups: carbonyl and hydroxyl - Highest carbonyl index (1.33) (3 L min^{-1} O_3)	[37]
Fenton, heat-activated persulfate and ozonation	LDPE (<500 μm)	–	$C_{cont} = 5$ g L^{-1} Fenton: $[Fe^{2+}]_0 = 1$ mM, $[H_2O_2]_0 = 10$ mM, $pH_0 = 3$, T = 25 °C Heat-activated persulfate: $[Persulfate]_0 = 100$ mM, pH_0 = not adjusted, T = 70 °C Ozonation: $[O_3]_0 = 0.21$ mg min^{-1} (flow rate 30 mL min^{-1}), pH_0 = not adjusted	- Pigment release and degradation by oxidation - HPLC - AFM-IR Topographical imaging. Nanoscale thermal analysis. Lorentz contact resonance	After 6 h reaction time: - Degradation rate of pigments is much faster than their leaching rate - Fragmentation and cracks, and rougher surfaces after treatment - Increase of height range (> 200%) for treated samples - Glass transition temperature decreased after treatment (except Fenton system) - MPs were softer after ozonation but stiffer after Fenton and persulfate treatments	[38]

UV-irradiance of 200 W m^{-2}, measured with a broad-range photo--radiometer (Delta Ohm, model HD 2102.1). The photoreactor was placed on a heating plate (IKA RCT Basic, Germany) under magnetic stirring at 500 rpm and operated at ambient conditions (25 °C and 1 atm). Photo-Fenton experiments were performed considering the impact of the main operating conditions, namely initial PS concentration (20 and 100 mg L^{-1}) of monodisperse PS nanospheres ($D_0 = 140$ nm), iron concentration (0.5 – 5 mg L^{-1}), initial pH ($pH_0 = 3$ and 5) and H_2O_2 concentration (130 – 260 mg L^{-1}). In all cases, the initial pH of the suspension was adjusted to the required value by using HNO_3, and the experiments were performed until reaching complete Total Organic Carbon (TOC) removal or a reaction time of 60 – 90 min. Under optimized operating conditions, the influence of the particle size was evaluated for PS nanospheres of $D_0 = 909$ nm. It should be noted that iron was fed as Fe^{3+} instead of Fe^{2+}, leading to a combination of photo-Fenton and Fenton-like processes to initiate the iron redox cycling [40–42]. Under the conditions studied, this resulted in a similar oxidation rate to the photooxidation of PS NPs carried out by feeding ferrous species (Fig. S1). Moreover, no formation of Fe precipitates was observed due to the enhancement of the Fe(III) photochemistry.

To distinguish the contribution of UV, UV/Fe^{3+}, UV/H_2O_2, and H_2O_2/ Fe^{3+} to the photo-Fenton reaction (UV/H_2O_2/Fe^{3+}), blank experiments were performed. Moreover, to confirm the contribution of hydroxyl radical to the degradation of PS NPs, the standard photo-

Table 2
Main properties of the commercial PS NPs tested in this work and theoretical stoichiometry for their oxidation.

	PS NPs	
Molecular structure	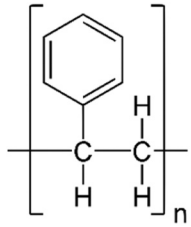	
TEM images	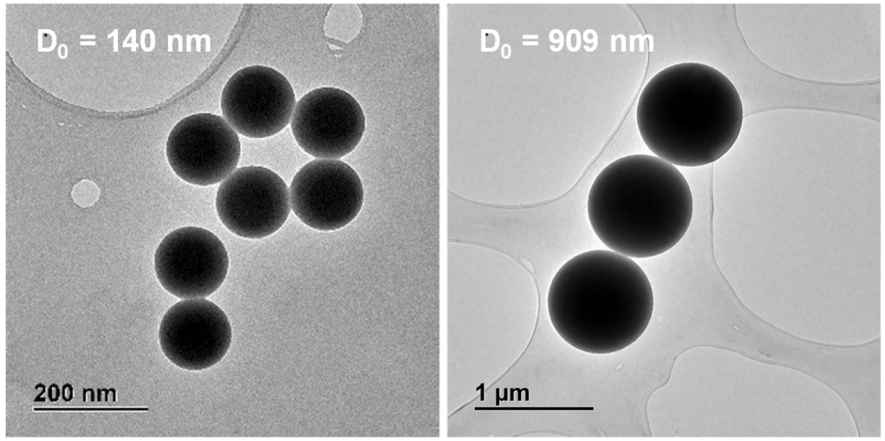	
Molecular weight (g mol^{-1}) and polydispersity index (PDI)	M_{w1} = 135324; PDI_1 = 1.48 M_{w2} = 3598; PDI_2 = 1.05	M_{w1} = 219,763; PDI_1 = 6.70 M_{w2} = 206,866; PDI_2 = 5.38
Melting point (°C)		74 – 105
Reaction	$[C_8H_8]_n + 20^*n\ H_2O_2 \rightarrow 8^*n\ CO_2 + 24^*n\ H_2O$	
H_2O_2 (mg L^{-1})*	130	

* Theoretical stoichiometric dose of H_2O_2 for the complete oxidation of PS nanospheres ($[PS\ NPs]_0$ = 20 mg L^{-1}).

Fenton experiment was conducted in the presence of 100 mmol L^{-1} IPA as a chemical scavenger [43,44]. All reaction experiments were performed in triplicate, and the standard deviation was less than 10% in all cases, represented as the error bars in the reported figures.

2.3. Analytical methods

The evolution of the oxidation reactions was followed by the analysis of Total Organic Carbon (TOC) using a TOC analyzer (Shimadzu TOC VSCH). It must be noted that the PS NPs tested in this work remained in a stable suspension in water, and thus, TOC analysis was an accurate method to determine their concentration. Turbidity was determined with a benchtop turbidity meter HI88713 (Hanna Instruments)·H_2O_2 and dissolved iron concentrations were measured by colorimetry using a Varian Cary 5000 UV–Visible Spectrophotometer, following the methods of titanium sulfate [45] and *o*-phenantroline [46], respectively.

The size of the NPs along the oxidation tests was determined by transmission electron microscopy (TEM) using a JEOL JEM 3000 F microscope with a 0.17 nm point resolution. The software "ImageJ" was used for measuring and counting the NPs particles (more than 100 particles per sample were considered). The M_W distribution of PS NPs was measured by gel permeation chromatography (GPC) (GPC 2414, Waters) with a Waters 2424 refractive index detector and a series of narrow polystyrene standards, using tetrahydrofuran as the mobile phase.

3. Results and discussion

3.1. Evaluation of UV, UV/Fe^{3+}, UV/H_2O_2, Fenton (H_2O_2/Fe^{3+}) and photo-Fenton (UV/H_2O_2/Fe^{3+}) systems for PS NPs oxidation

Fig. 1 shows the evolution of TOC upon the treatment of PS NPs by

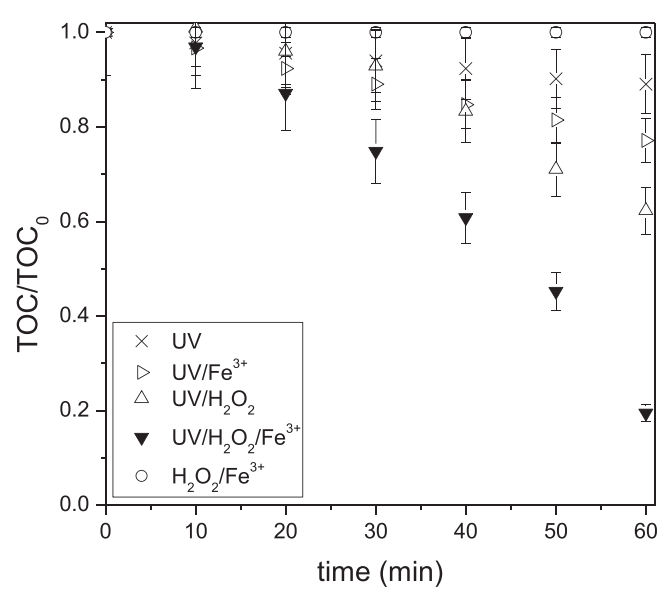

Fig. 1. Evolution of PS NPs (140 nm) mineralization upon UV, UV/Fe^{3+}, UV/H_2O_2, H_2O_2/ Fe^{3+}, and UV/H_2O_2/ Fe^{3+} treatments ($[PS\ NPs]_0$ = 100 mg L^{-1}; $[Fe^{3+}]_0$ = 2 mg L^{-1}; $[H_2O_2]_0$ = 1000 mg L^{-1}; pH_0 = 3 and T = 25 °C).

UV, UV/Fe^{3+}, UV/H_2O_2, *H_2O_2/Fe^{3+}*, and UV/H_2O_2/Fe^{3+}. All the runs were carried out at 25 ºC and $pH_0 = 3$. Clearly, PS NPs were susceptible to be attacked by the photons generated by UV irradiation. A mineralization yield of approximately 11% was achieved after 60 min reaction time through direct photolysis. The photodegradation is likely initiated by the phenolic rings of PS absorbing UV irradiation, leading to the generation of electronically excited states. In these states, the polymer undergoes intramolecular transformations and stabilizes states with different electron distributions, followed by decomposition to radicals [25,47]. Polystyryl radicals are expected to be formed [47]. Their reaction with oxygen likely leads to the generation of peroxy radicals, which undergo chain scission and form carbonyl compounds, that are further mineralized. Previous studies have reported the degradation of PS NPs exposed to UV irradiation, but considerably lower degradation yields were obtained, which can be attributed to the larger size of the PS NPs (~300 nm) tested, as well as the different irradiation sources (in terms of wavelength and light intensity) used (Table 1) [25,27]. All in all, direct photolysis of PS NPs was expected, as the slow degradation of PS polymers has been even confirmed even in the natural environment through solar irradiation [27].

The addition of homogeneous Fe led to a slightly higher mineralization yield of PS NPs compared to UV irradiation alone. In this case, 23% removal of TOC was reached after 60 min reaction time (Fig.1). This result can be explained by the photolysis of aquated ferric species (Eqs. (1) and (4)), available as Fe^{3+}, $Fe(OH)^{2+}$, and $Fe(OH)_2^+$, as well as Fe^{3+}-complexes (Eq. (2)), which can generate hydroxyl radicals and oxidize the target pollutant [40,48]. The application of UV/H_2O_2 significantly enhanced the kinetics and mineralization yield of PS NPs (Fig. 1). Almost 40% of TOC was completely oxidized to CO_2 after 60 min reaction time. The improvement is attributed to the photolysis of H_2O_2 (Eq. (3)), which directly generates hydroxyl radicals [40,48]. Consistent with these results, the photo-Fenton process was clearly the most effective treatment, achieving over 80% mineralization of PS NPs within a 60 min reaction time (Fig. 1). In this system, in addition to the photodecomposition of H_2O_2 (Eq. (3)) and the photosensitization of aquated ferrous/ferric complexes (Eqs. (1), (2) and (4)), Fenton reactions (Eqs. (5) and (6)) act as additional sources of hydroxyl and hydroperoxyl radicals [40,48]. The improvement in the system is primarily attributed to the photochemistry of Fe(III) (Eqs. (1), (2) and (4)), where Fe(III) complexes undergo ligand to-metal charge transfer excitation, leading to dissociation into Fe(II) and an oxidized ligand (L_{ox}) (Eq. (2)). For comparative purposes, the classic Fenton process was evaluated in the absence of light, resulting in no measurable removal of TOC under the studied conditions (Fig. 1). Our recent research confirms that the mineralization of PS NPs requires harsher operating conditions and a higher catalyst concentration in the absence of light [35]. Finally, the experiment with IPA as chemical scavenger of HO• confirmed its key role in the degradation of PS NPs (Fig. S2). Based on these results, the photo-Fenton process was selected for further optimization to improve its efficiency.

$$Fe^{3+} + H_2O + h\nu \rightarrow Fe^{2+} + H^+ + HO\cdot \quad (1)$$

$$Fe^{3+}(L)_n + h\nu \rightarrow Fe^{2+}(L)_{n-1} + L\cdot_{ox} \quad (2)$$

$$H_2O_2 + h\nu \rightarrow 2HO\cdot \quad (3)$$

$$[Fe(HO_2)]^{2+} + h\nu \rightarrow Fe^{2+} + HO_2\cdot \quad (4)$$

$$Fe^{2+} + H_2O_2 \rightarrow Fe^{3+} + HO\cdot + OH^- \quad (5)$$

$$Fe^{3+} + H_2O_2 \rightarrow Fe^{2+} + HO_2\cdot + H^+ \quad (6)$$

The high mineralization yield of PS NPs through photo-Fenton oxidation can be favorably compared with the results previously reported in the literature (Table 1). Most studies only reported partial degradation of MPs/NPs and the formation of wrinkles, cracks, and cavities on their surface, along with the generation of oxygen functional groups. Importantly, achieving high levels of mineralization did not require any surface pretreatment of the PS nanospheres. Up to now, photocatalysis was the most extensively studied process, but at the most 50% mineralization of PS NPs was achieved in aqueous phase at ambient conditions [26,27]. Furthermore, the photo-Fenton process, based on the use of diluted homogeneous Fe species, offers a significant practical advantage over photocatalysis, which is clearly limited by the challenges of catalyst recovery and mass transfer limitations due to the slower diffusion rates of solid pollutants to the surface of heterogeneous catalysts.

3.1.1. Proposed mechanisms for photodegradation of PS reported in previous studies

Different authors have reported the photodegradation mechanism of PS, considering both the photooxidative reactions occurring on the PS surface and the leaching of water-soluble oxidation products into the liquid phase. Among them, Ainali et al. conducted a study on the degradation of PS films under UV irradiation at 280 nm and 25 °C in air. They observed significant morphological changes, including the development of cracks and holes on the PS surface. Pyr-GC/MS analysis revealed the formation of ketones, aldehydes, alcohols, lactones, and cyclization products [49]. However, it is important to note that the phototransformation mechanisms of PS can differ in air and water matrices [50]. Cao et al. reported a photocatalytic method for oxidizing PS to aromatic oxygenates in the liquid phase using a g-C_3N_4 catalyst and oxygen under visible light irradiation at 150 ºC and 10 bar. They proposed a reaction pathway involving chain oxidation, activation of C–H bonds, bond scission (C–C bond activation), and further oxidation leading mainly to benzoic acid through a radical mechanism. The oxidation intermediates identified included p-isopropylphenol, ethylbenzene, sec-butylbenzene-like molecules, benzaldehyde, acetophenone, and CO_2. Interestingly, the solid components in the reaction mixture exhibited an increase in molecular weight instead of depolymerizing into PS intermediates with shorter chains, possibly due to the introduction of oxygen-functional groups onto the PS lattice and/or re-polymerization induced by radical attack [51]. Domíngues-Jaimes et al. investigated the photocatalytic degradation of PS NPs (D_0 = 315 nm) with TiO_2 catalysts. They observed chain scission, formation of a carbonyl group (2-Butanone, 3,3-dimethyl), rupture of the aromatic ring (2-[3-Methylbuta-1,3-dienyl] cyclohexanone), and the formation of two other intermediates with carbonyl groups resulting from the union and cross-linking of a cyclic compound. The authors suggested that these compounds could be completely mineralized with extended reaction time [25]. Bianco et al. examined the reactivity of HO• radicals towards the photolysis and photolysis of H_2O_2 applied to PS NPs (D_0 = 400 nm) in the liquid phase. They observed the formation of carboxylic compounds such as formic, acetic, and lactic acids, as well as aromatic acids like benzoic acid, along with aliphatic and aromatic aldehydes such as muconaldehyde and benzaldehyde. Additionally, they identified benzoquinone, dibenzoyl methane, and benzoic anhydride as by-products of photodegradation. The formation of these intermediates was attributed to the generation of tertiary polystyryl radicals through HO• addition to π-systems or hydrogen abstraction [52]. Tian et al. investigated the photodegradation of PS NPs (D_0 = 250 nm) under UV-C irradiation in air and water matrices. In the liquid phase, photo-oxidative degradation resulted in chain scission and cross-linking, leading to the formation of active functional groups on the PS NPs surface (confirmed by XPS measurements). Smaller molecules could undergo further degradation to form water-soluble compounds or mineralized to CO_2. The authors demonstrated that the presence of pure water promoted the photo-oxidation and mineralization of PS NPs while reducing cross-linking induced by UV irradiation. Several possible reaction mechanisms were proposed. Firstly, water absorbed the excess energy, which could produce overloaded R• for cross-linking. Additionally, light scattering by the suspended NPs and water molecules increased the exposure area, enhancing the chances of R• reacting with O_2 or HO•. Secondly, water

could directly react with R• or ROO• radicals, leading to the formation of alkoxy polymer radicals (RO•) that could undergo further chain scission under UV irradiation. Thirdly, hydroxyl radicals could form in water and accelerate subsequent degradation and mineralization processes. Alongside the photo-oxidative reactions occurring on the surface of PS NPs, water-soluble products were also formed. Small molecules with condensed aromatic rings, having side-chains with –OH and C═O groups, or oxidized monomers with single benzene rings, were continuously released from the polymer into the surrounding water. These dissolved molecules in water had the potential to undergo further degradation, ultimately resulting in the production of CO_2 [50]. García Muñoz et al. conducted a study on the photocatalytic degradation of PS NPs ($D_0 = 140$, 300, and 525 nm), reporting the formation of acetic acid, benzoic acid, and benzophenone. The authors proposed a reaction mechanism in which the photocatalytic reaction is initiated by the attack of HO• radicals on PS particles. This attack generates carbon-centered radicals within the polymer structure and can occur simultaneously on multiple carbon atoms. Subsequently, these radicals can react with dissolved oxygen, leading to the formation of peroxide molecules. The third step possibly involves the production of hydroperoxide compounds when peroxide interacts with water molecules. Further reactions can result in chain scission and the formation of carbonyl or ketone compounds. These intermediates can then undergo further degradation to CO_2 and water. It is important to note that UV photons can directly be absorbed by the polymeric chains, creating excited states that generate chain scission, cross-linking, and polymer oxidation [53].

3.2. Operating conditions study for the photo-Fenton oxidation of PS nanoplastics

The impact of the main variables of the process, namely initial PS NPs concentration, catalyst concentration, initial pH, and H_2O_2 dose, was systematically evaluated.

Firstly, the photo-Fenton process was evaluated at different initial concentrations of the target pollutant in the range 20 – 100 mg L^{-1}, at $[Fe^{3+}]_0 = 2$ mg L^{-1}, $[H_2O_2]_0$ / $[PS\ NPs]_0 = 10$, $pH_0 = 3$ and 25 °C (Fig. 2). For an initial concentration of 20 mg L^{-1}, PS NPs were completely mineralized after 40 min of photo-Fenton treatment under ambient conditions. Meanwhile, the treatment of $[PS\ NPs]_0 = 100$ mg L^{-1} achieved more than 80% mineralization after 60 min reaction time (Fig. 2A). Clearly, the photo-Fenton process exhibits outstanding performance at ambient conditions and can be applied to different loads of PS NPs, demonstrating its feasibility across a broad range of concentrations. Likewise, the evolution of TOC or mineralization appears to follow a first-order kinetic equation (Fig. 2B). On one hand, it can be observed that the mineralization process of 100 mg L^{-1} PS NPs starts slowly and increases its rate after approximately 30 min reaction time. If the oxidation process is divided in two phases, pseudo-first-order rate constant values of $k_{100,1} = 0.0098$ min^{-1} ($R^2 = 0.93$) and $k_{100,2} = 0.0435$ min^{-1} ($R^2 = 0.90$) were obtained for the first and second phase, respectively. The subscripts numbers in the constants indicate the main condition under consideration (initial PS concentration) and the corresponding reaction phase. On the other hand, the oxidation of 20 mg L^{-1} PS NPs was faster, achieving a pseudo-first-order rate constant value of $k_{20} = 0.0934$ min^{-1} ($R^2 = 0.95$). Consequently, when higher PS concentrations are treated, the rate of TOC removal slows down, likely due to both an increased surface area available to be attacked by radicals and a lower irradiance reaching the NPs surface [29].

To investigate more in depth the role of initial PS NPs concentration on the photo-Fenton performance, turbidity measurements and TEM analysis were carried out. From preliminary calibration curves, it was demonstrated that the turbidity of the reaction medium increases with both the NPs concentration and the particle size (see Fig. S3 in the Supplementary Information). From Fig. 2C, it can be observed that the

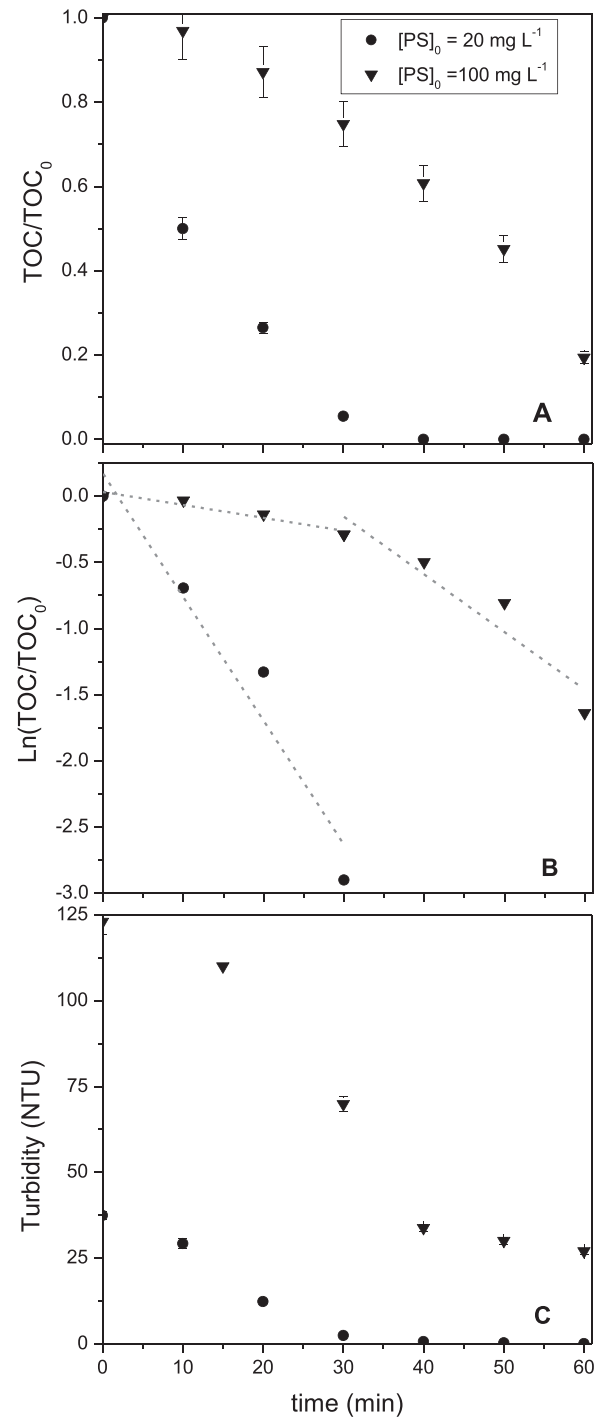

Fig. 2. Photo-Fenton oxidation of PS NPs (140 nm) at different initial concentrations of the target pollutant: a) TOC evolution, b) pseudo-first-order adjustment and c) turbidity evolution ($[Fe^{3+}]_0 = 2$ mg L^{-1}; $[H_2O_2]$ / $[PS\ NPs]_0 = 10$; $pH_0 = 3$; T = 25 °C).

turbidity of the reaction medium decreased from its initial value until reaching a completely clear solution after 40 min of photo-Fenton treatment with $[PS\ NPs]_0 = 20$ mg L^{-1}, under the conditions considered (see Fig. S4 in the Supplementary Information). With $[PS\ NPs]_0 = 100$ mg L^{-1}, a very similar trend was observed but, in this case, the turbidity reduction only reached 78% after 60 min reaction time under the same operating conditions. The trends observed in the turbidity evolution are directly related to the advance of PS NPs oxidation and decrease in particle size. Fig. 3 displays the TEM micrographs for

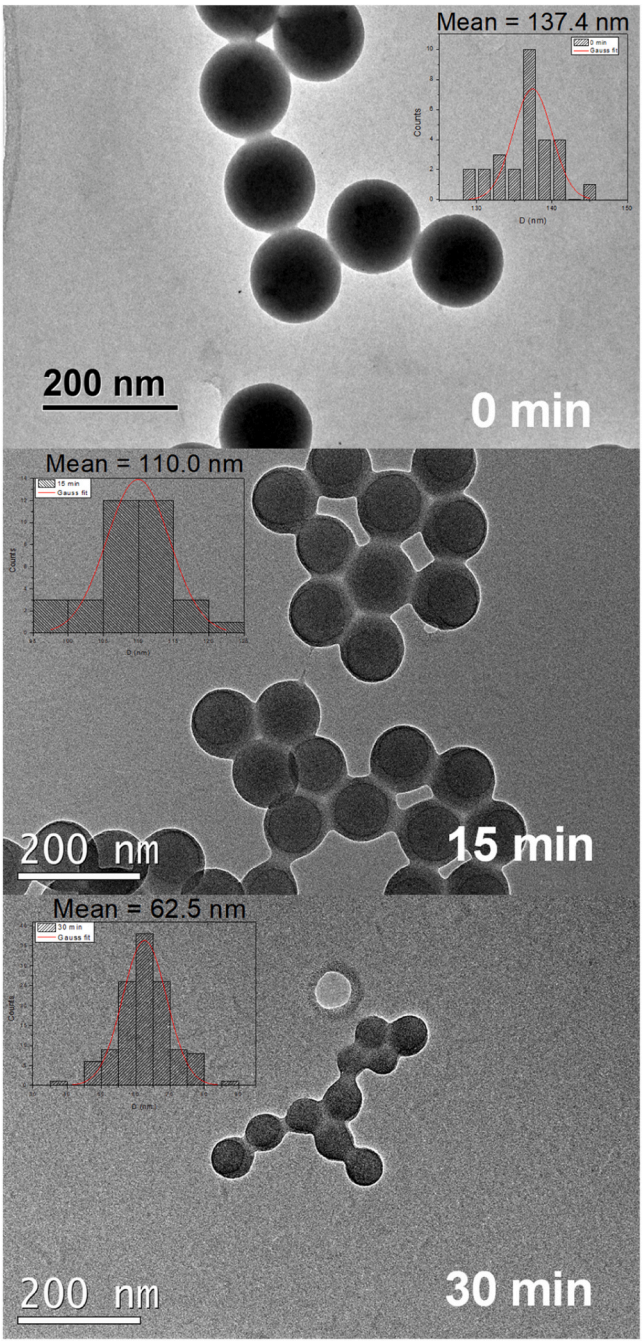

Fig. 3. TEM analysis for the photo-Fenton oxidation of PS NPs (140 nm) ([PS NPs]$_0$ = 20 mg L^{-1}; [Fe^{3+}]$_0$ = 2 mg L^{-1}; [H_2O_2]$_0$ = 200 mg L^{-1}; pH$_0$ = 3; T = 25 °C).

samples withdrawn at different reaction times with an initial concentration of PS NPs of 20 mg L^{-1} (see Fig. S5 of the Supporting Information for TEM micrographs obtained with [PS NPs]$_0$ = 100 mg L^{-1}). At initial times, the reaction medium consists mainly of inert polystyrene nanoparticles that are hardly degradable; as the photo-oxidation proceeds, new surface functionalities begin to appear due to the breakdown of polymeric chains by the radicals attack favoring the particles agglomeration/assembly through their superficial adhesion and chain cross-linking [47]. This mechanism can be inferred by both the fading of particles boundaries and the formation of bridges between nanospheres (Figs. 3 and S5). As the reaction proceeds, these agglomerates reduce their size, as well as the individual particle's size decreases (Tables S1 and S2), in accordance with the turbidity measurements. At 30 min reaction time with 20 mg L^{-1} PS NPs, individual particles achieved a mean diameter of 62.5 nm and a volume reduction of 90.5%; beyond that time, no particle's agglomerates were identified in the reaction medium (Table S1). While at 60 min reaction time with 100 mg L^{-1} PS NPs, individual particles achieved a mean diameter of 88.7 nm and a volume reduction of 72.9% (Table S2). Furthermore, despite the formation of agglomerates, the particles were oxidized from the surface to the core, retaining their sphericity and increasing the particle size distribution. This result can be explained by the fact that HO• would react with the PS surface sites (most likely, the aromatic rings) without access to the polymer bulk [52]. Finally, TEM images also show that individual nanospheres display two densities in their composition, glimpsed by two areas with different contrast in the images. This fact might be related to the synthesis procedure and/or to the bimodal distribution of the polymer's molecular weight (Table 2). Therefore, the surface/shell and the core of the PS nanospheres could exhibit different reactivity degrees towards the applied photo-oxidative treatment.

Regarding hydrogen peroxide consumption (not shown), complete conversion of the oxidant was achieved after 30 min and 60 min reaction time for 20 mg L^{-1} and 100 mg L^{-1} of PS NPs, respectively.

From these results, the photo-Fenton treatment is projected to be highly efficient for the treatment of lower NPs concentrations, such as those expected in a WWTP. Therefore, to work in more realistic conditions, the screening of operating conditions was continued by using an initial concentration of 20 mg L^{-1} of PS NPs.

The amount of catalyst added to the reactor is a critical issue in the application of Fenton-like processes [35,54]. Fig. 4 shows the values of the pseudo-first-order rate constants upon photo-Fenton oxidation of PS at different initial Fe^{3+} concentrations in the range 0.5 – 5 mg L^{-1}, at [PS NPs]$_0$ = 20 mg L^{-1}, [H_2O_2]$_0$ = 130 mg L^{-1}, pH$_0$ = 3 and 25 °C. As can be observed, the highest initial rate of TOC removal was achieved by using 1 mg L^{-1} Fe^{3+}, while complete mineralization was achieved for all catalyst concentrations tested after 40 – 50 min reaction time. Beyond 1 mg L^{-1} Fe^{3+}, the initial mineralization rate was slowed down probably due to a radical's scavenging effect with the excess of Fe species, while below this value, the initial rate was decelerated due to a low concentration of the homogeneous catalyst [54]. Unlike the classic Fenton process [35], irradiation with wavelengths below 580 nm enables the reduction of iron concentration, resulting in a significantly faster regeneration of the ferrous species and preventing the formation of sludge [39]. Likewise, the possibility of using low Fe concentrations,

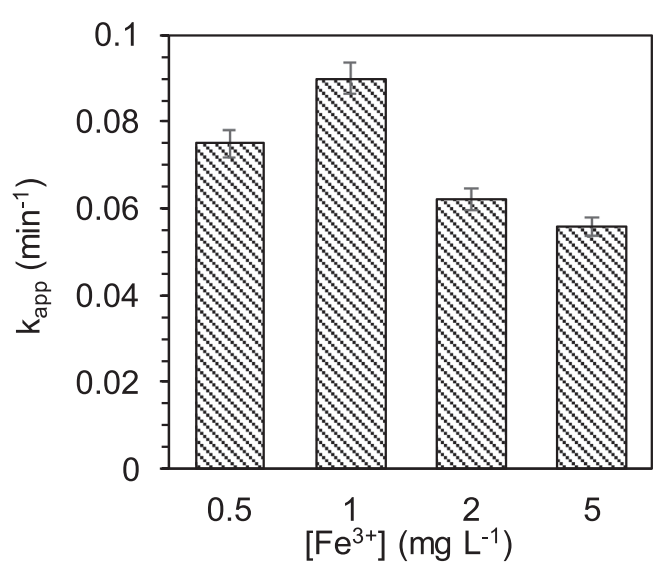

Fig. 4. Values of the pseudo-first-order rate constants upon photo-Fenton oxidation of PS NPs (140 nm) at different Fe^{3+} concentrations ([PS NPs]$_0$ = 20 mg L^{-1}; [H_2O_2]$_0$ = 130 mg L^{-1}; pH$_0$ = 3; T = 25 °C).

such as 1 mg L^{-1}, is particularly interesting since it is below the limit of iron concentration (2 mg L^{-1}) stablished in the EU directive for treated water [55] and consequently, there is no need to separate the homogeneous catalyst after treatment, which is advantageous with a view to reclaimed water applications [56].

The influence of pH on the photo-Fenton oxidation of PS NPs can be seen in Fig. 5 ([PS NPs]$_0$ = 20 mg L^{-1}; [Fe^{3+}]$_0$ = 1 mg L^{-1}; [H_2O_2]$_0$ = 130 mg L^{-1} and T = 25 °C). It is clearly observed that the acidic pH favors the yield of the photo-Fenton process. In fact, operating at pH 3 is generally accepted as the optimal pH value for classical Fenton's oxidation process [40]. Under this condition, the mineralization yield achieved > 99% in 40 min reaction time, while operating at pH 5 reached up to 92%. In agreement with these results, the apparent pseudo-first-order rate constant values were k_{pH3} = 0.090 min^{-1} (R^2 = 0.98) and k_{pH5} = 0.050 min^{-1} (R^2 = 0.92), respectively. It should be highlighted that no yellowish colloids were observed macroscopically in the reaction volume when operating at pH 5, discarding the presence of relatively inactive hydrous oxyhydroxides of Fe. As was explained previously, it is expected that the photoassisted process prevented the formation of Fe precipitates due to an improved redox cycle between ferrous/ferric species [39]. Moreover, it is widely known that parasitic decomposition of hydrogen peroxide increases sharply above pH 5 [40]. Therefore, it is expected a more inefficient use of the oxidant by operating at pH 5. Nevertheless, the possibility of achieving high conversion levels by operating at circumneutral pH values can be considered a practical advantage. Although it is beyond the scope of this work, working at a neutral pH can be accomplished by incorporating iron chelating agents [57]. In any case, the efficiency of this process must be compared with the yield of UV/H_2O_2 under similar operating conditions [17].

The impact of the H_2O_2 dose on the mineralization of PS NPs was investigated in the range of 130 – 260 mg L^{-1} (Fig. 6). The supra-stoichiometric H_2O_2 dose (260 mg L^{-1}) led to complete mineralization of PS NPs after 30 min reaction time, while using the stoichiometric dose took 40 min reaction time. This slight difference in the mineralization yield was due to the total consumption of the hydrogen peroxide after 30 min of photo-Fenton treatment using [H_2O_2]$_0$ = 130 mg L^{-1} (Fig. 6B). Consequently, the only source of radicals in the system between 30 and 40 min reaction time was the photolysis of dissolved iron

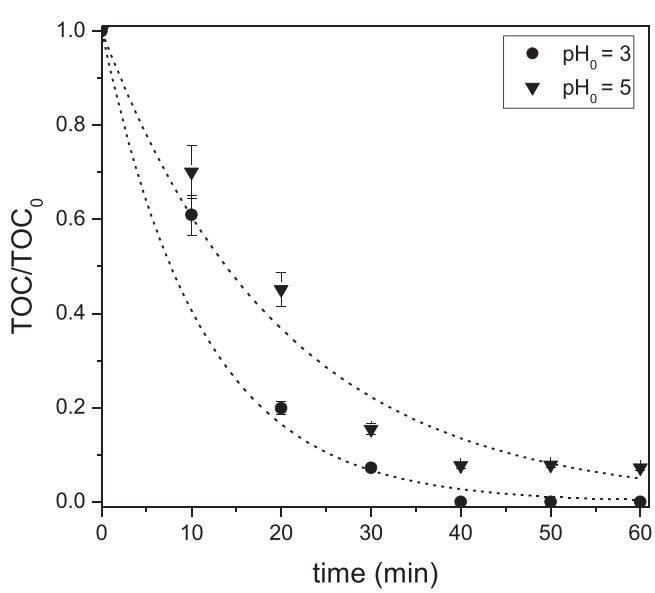

Fig. 5. Evolution of TOC upon photo-Fenton oxidation of PS NPs (140 nm) at different pH values ([PS NPs]$_0$ = 20 mg L^{-1}; [Fe^{3+}]$_0$ = 1 mg L^{-1}; [H_2O_2]$_0$ = 130 mg L^{-1}; T = 25 °C). The dashed lines represent the pseudo-first-order approximation.

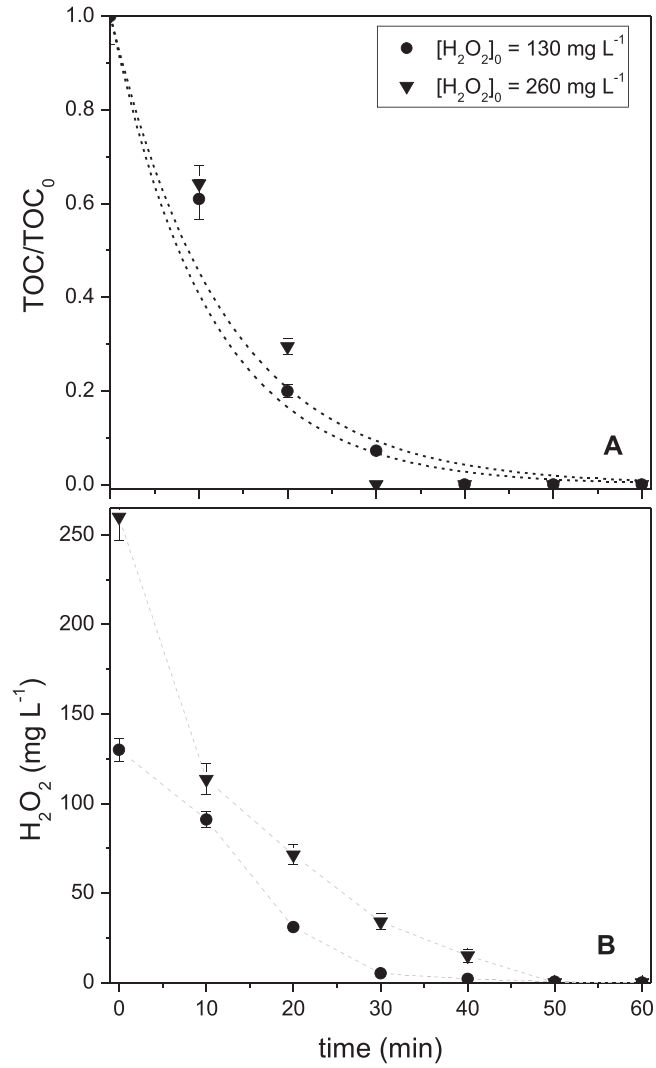

Fig. 6. Photo-Fenton oxidation of PS NPs (140 nm) at different H_2O_2 doses: a) TOC evolution and b) H_2O_2 evolution ([PS NPs]$_0$ = 20 mg L^{-1}; [Fe^{3+}]$_0$ = 1 mg L^{-1}; pH$_0$ = 3; T = 25 °C). The dashed lines in dimensionless TOC removal represent the pseudo-first-order approximation.

species (Eqs. (1), (2) and (4)). Additionally, the pseudo-first-order kinetic fitting displayed a lower constant rate (k_{260} = 0.079 min-1; R2 = 0.96) compared to the stoichiometric dosage (k_{130} = 0.090 min^{-1}; R^2 = 0.98). This fact might be related with the development of parasitic reactions with the excess of hydrogen peroxide in the first minutes of the photo-oxidation test using 260 mg L^{-1} H_2O_2 [17,40,54]. Subsequently, the efficiencies of hydrogen peroxide consumption (η) were evaluated according to Zazo et al., where η_i (mg TOC/g H_2O_2 converted) is defined as the amount of TOC converted per unit weight of hydrogen peroxide decomposed [58], and 'i' stands for the initial H_2O_2 concentration employed. The efficiencies reached at different H_2O_2 doses were: η_{130} = 142 and η_{260} = 71 mg TOC/g H_2O_2 converted, considered at final reaction time. All in all, the hydrogen peroxide dose must be properly adjusted since excessive oxidant doses can scavenge HO• and dramatically increase the cost of the process. On the other hand, if the H_2O_2 concentration is insufficient, the oxidation progress can be hindered [17]. In this sense, to minimize parasitic reactions with the oxidant and enhance the oxidation rate, dosage strategies for H_2O_2, such as continuous supply or multiple-step addition of the oxidant, may be beneficial.

In summary, the photo-Fenton process shows great potential to produce high-quality reclaimed water. The optimal dosages of Fe^{3+} and

H_2O_2 were 1 mg L^{-1} and 130 mg L^{-1}, respectively. These values are consistent with the reported catalyst and oxidant doses used for the removal of dissolved organic pollutants [39,59], as well as the efficiency in hydrogen peroxide consumption [41]. Additionally, the system can be operated at ambient conditions, significantly reducing the operating costs. Another notable feature is the possibility of achieving almost complete elimination of PS NPs at pH 5, reducing the concentration of reagents required for acidifying the influent and neutralizing the treated water.

3.3. Impact of PS nanoplastic size on the performance of the process

To further demonstrate the feasibility of the photo-Fenton process for the removal of PS NPs in water, the treatment was applied to PS nanospheres with a diameter of 909 nm. Experimental results carried out under optimized operating conditions: $[PS\ NPs]_0 = 20$ mg L^{-1}; $[Fe^{3+}]_0 = 1$ mg L^{-1}; $[H_2O_2]_0 = 130$ mg L^{-1}; $pH_0 = 3$ and T = 25 ºC are shown in Figs. 7 and 8. Due to the irradiation source employed, hydrogen peroxide was completely depleted after 30 min reaction time, regardless of the particle size (as depicted in Fig. 6B). To further enhance the mineralization yield with the larger PS nanospheres, two additional stoichiometric doses of 130 mg L^{-1} H_2O_2 were added every 30 min once the oxidant was completely depleted. As observed, PS nanospheres of 909 nm were mineralized at a slower rate compared to the smaller nanoparticles with a nominal diameter of 140 nm. Pseudo-first-order rate constants of $k_{140} = 0.090\ min^{-1}$ ($R^2 = 0.98$) and $k_{909} = 0.032\ min^{-1}$ ($R^2 = 0.97$) were achieved. As the particle size decreases, the surface-to-volume ratio increases significantly, leading to a greater surface reactivity, exposing higher values of surface area to the attack by HO• radicals followed by oxidation [52]. This result is consistent with our previous study on the degradation of PS MPs/NPs by Fenton oxidation. It suggests that the reaction occurs initially on the surface of the NPs and proceeds towards the core of the plastic particles [35]. Moreover, the turbidity of the solution also decreases (Fig. S3), and the suspension of smaller particles receives more irradiance on their surface, resulting in faster mineralization.

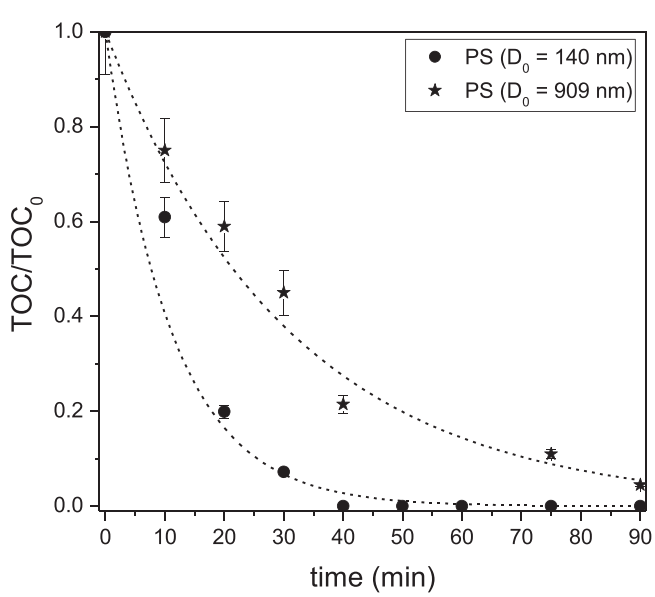

Fig. 7. Evolution of TOC upon photo-Fenton oxidation of PS NPs of different particle sizes ($[PS\ NPs]_0 = 20$ mg L^{-1}; $[Fe^{3+}]_0 = 1$ mg L^{-1}; $[H_2O_2]_0 = 130$ mg L^{-1}; $pH_0 = 3$; T = 25 ºC). The dashed lines represent the pseudo-first-order approximation.

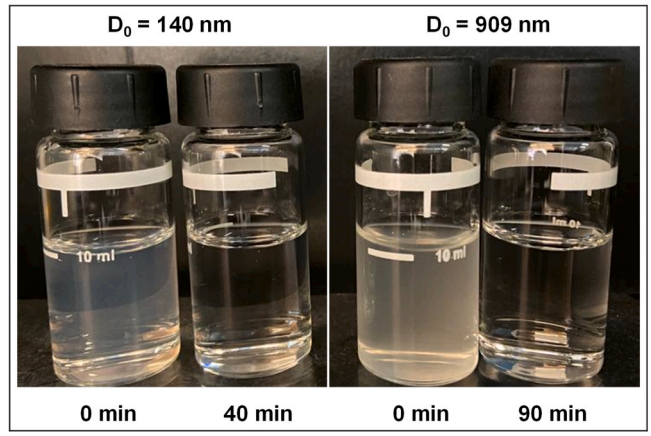

Fig. 8. Visual inspection of the reaction volume turbidity without treatment and at final reaction time upon photo-Fenton oxidation of PS NPs of different particle size ($[PS\ NPs]_0 = 20$ mg L^{-1}; $[Fe^{3+}]_0 = 1$ mg L^{-1}; $[H_2O_2]_0 = 130$ mg L^{-1}; $pH_0 = 3$; T = 25 ºC).

4. Conclusions

The photo-Fenton process, using broad-spectrum UV-irradiance ranging from 250 to 600 nm as the light source and diluted homogeneous Fe species, has proved to be highly effective in completely mineralizing polystyrene (PS) nanoplastics (NPs) in water under ambient conditions. The oxidation process begins at the particle surface (most likely, the phenolic rings of PS), leading to the formation of new functionalities and the breakdown of polymeric chains through the hydroxyl radical attack. This process promotes the agglomeration and assembly of particles through superficial adhesion and chain crosslinking. As the oxidation progresses from the surface to the core of the NPs, these agglomerates decrease in size along with individual particle size, leading to a reduction in turbidity until complete disappearance.

Optimized conditions ($[PS\ NPs]_0 = 20$ mg L^{-1}; $[Fe^{3+}]_0 = 1$ mg L^{-1}; $[H_2O_2]_0 = 130$ mg L^{-1}; $pH_0 = 3$ and T = 25 ºC) achieved complete mineralization (>99% TOC removal) and rapid degradation of PS NPs (140 nm) in 40 min reaction time, exhibiting a pseudo-first-order rate constant of 0.090 min^{-1} ($R^2 = 0.98$) and an efficiency of hydrogen peroxide consumption of 142 mg TOC/g H_2O_2 converted. The outstanding performance of the photo-Fenton process can be attributed to the wavelength range and light intensity employed, surpassing the removal levels of the photocatalytic processes reported in the literature. The concentration and particle size of NPs significantly influenced the mineralization rate, but complete degradation of larger particles or concentrated solutions can be attained by increasing the dose of hydrogen peroxide and extending reaction time.

Based on these findings, the implementation of photo-Fenton treatment using diluted homogeneous Fe concentrations holds great potential as a purification step in tertiary treatments. This process could be combined with conventional separation processes, such as membrane filtration, to treat concentrate streams and facilitates the mineralization of NPs at wastewater treatment plants (WWTPs). By integrating advanced treatments, such as the photo-Fenton process, into the existing treatment feasibilities, the dispersion and impact of MPs/NPs can be substantially minimized, ensuring the production of cleaner reclaimed water. Although modified Fenton processes have demonstrated improved oxidative performances for the removal of MPs/NPs, research on these technologies is still in its early stages and requires further in-depth study to establish them as viable options for implementation in actual WWTPs.

CRediT authorship contribution statement

Carla di Luca: Conceptualization, Methodology, Investigation, Formal analysis, Writing – original draft, Writing – review & editing, Visualization. **Jorge Garcia:** Methodology, Validation, Investigation. **David Ortiz:** Methodology, Investigation. **Macarena Munoz:** Conceptualization, Formal analysis, Writing – original draft, Writing – review & editing, Supervision, Project administration, Funding acquisition. **Jaime Carbajo:** Methodology, Writing – review & editing. **Zahara M. de Pedro:** Conceptualization, Writing – review & editing, Supervision, Project administration, Funding acquisition. **Jose A. Casas:** Conceptualization, Writing – review & editing, Supervision, Project administration, Funding acquisition.

Declaration of Competing Interest

The authors declare the following financial interests/personal relationships which may be considered as potential competing interests: Carla di Luca reports financial support was provided by European Commission.

Data availability

Data will be made available on request.

Acknowledgments

This research has been supported by the Autonoma University of Madrid and Community of Madrid through the project SI1-PJI-2019–00006, and by the Spanish Ministry for Science and Innovation (MICINN) through the projects PID2019–105079RB-I00 and TED2021–131380B-C21. C. di Luca thanks financial support from the European Union's Horizon Europe research and innovation programme under the Marie Skłodowska Curie postdoctoral grant agreement Nº: 101062665. D. Ortiz thanks the Spanish MIU for the FPU predoctoral grant (FPU19/04816). M. Munoz thanks the Spanish MINECO for the Ramón y Cajal postdoctoral contract (RYC-2016–20648).

Appendix A. Supporting information

Supplementary data associated with this article can be found in the online version at doi:10.1016/j.jece.2023.110755.

References

[1] Plastics Europe, Plastics – the Facts 2022 An analysis of European plastics production, demand, conversion and end-of-life management, 2022. Available in: ⟨https://plasticseurope.org/knowledge-hub/plastics-the-facts-2022/⟩.
[2] D.E. MacArthur, D. Waughray, R.M. Stuchtey, The new plastics economy: rethinking the future of plastics, World Econ. Forum (2016) (Available in), ⟨https://www3.weforum.org/docs/WEF_The_New_Plastics_Economy.pdf⟩.
[3] M. Enfrin, L.F. Dumée, J. Lee, Nano/microplastics in water and wastewater treatment processes – Origin, impact and potential solutions, Water Res. 161 (2019) 621–638, https://doi.org/10.1016/j.watres.2019.06.049.
[4] A. Forrest, L. Giacovazzi, S. Dunlop, J. Reisser, D. Tickler, A. Jamieson, J. J. Meeuwig, Eliminating Plastic Pollution: How a Voluntary Contribution From Industry Will Drive the Circular Plastics Economy, Front. Mar. Sci. 6 (2019), 627, https://doi.org/10.3389/fmars.2019.00627.
[5] M. Oliveira, M. Almeida, The why and how of micro(nano)plastic research, Trends Anal. Chem. 114 (2019) 196–201, https://doi.org/10.1016/j.trac.2019.02.023.
[6] I. Ali, T. Ding, C. Peng, I. Naz, H. Sun, J. Li, J. Liu, Micro- and nanoplastics in wastewater treatment plants: Occurrence, removal, fate, impacts and remediation technologies – A critical review, Chem. Eng. J. 423 (2021), 130205, https://doi.org/10.1016/j.cej.2021.130205.
[7] C. Bretas Alvim, J.A. Mendoza-Roca, A. Bes-Piá, Wastewater treatment plant as microplastics release source – Quantification and identification techniques, J. Environ. Manag. 255 (2020), 109739, https://doi.org/10.1016/j.jenvman.2019.109739.
[8] A.A. Koelmans, E. Besseling, W.J. Shim, Nanoplastics in the aquatic environment. Critical review, in: M. Bergmann, L. Gutow, M. Klages (Eds.), Marine Anthropogenic Litter, Springer, Cham, 2015, pp. 325–340, https://doi.org/10.1007/978-3-319-16510-3_12.
[9] S. Singh, T.S.S. Kumar Naik, A.G. Anil, J. Dhiman, V. Kumar, D.S. Dhanjal, L. Aguilar-Marcelino, J. Singh, P.C. Ramamurthy, Micro (nano) plastics in wastewater: A critical review on toxicity risk assessment, behaviour, environmental impact and challenges, Chemosphere 290 (2022), 133169, https://doi.org/10.1016/j.chemosphere.2021.133169.
[10] S.A. Strungaru, R. Jijie, M. Nicoara, G. Plavan, C. Faggio, Micro- (nano) plastics in freshwater ecosystems: Abundance, toxicological impact and quantification methodology, Trends Anal. Chem. 110 (2019) 116–128, https://doi.org/10.1016/j.trac.2018.10.025.
[11] Y. Zhang, Y. Li, F. Su, L. Peng, D. Liu, The life cycle of micro-nano plastics in domestic sewage, Sci. Total Environ. 802 (2022), 149658, https://doi.org/10.1016/j.scitotenv.2021.149658.
[12] D. Sol, A. Laca, A. Laca, M. Díaz, Approaching the environmental problem of microplastics: Importance of WWTP treatments, Sci. Total Environ. 740 (2020), 140016, https://doi.org/10.1016/j.scitotenv.2020.140016.
[13] Z. Xu, X. Bai, Z. Ye, Removal and generation of microplastics in wastewater treatment plants: A review, J. Clean. Prod. 291 (2021), 125982, https://doi.org/10.1016/j.jclepro.2021.125982.
[14] A. Giwa, A. Yusuf, H.A. Balogun, N.S. Sambudi, M.R. Bilad, I. Adeyemi, S. Chakraborty, S. Curcio, Recent advances in advanced oxidation processes for removal of contaminants from water: A comprehensive review, Process Saf. Environ. Prot. 146 (2021) 220–256, https://doi.org/10.1016/j.psep.2020.08.015.
[15] D.B. Miklos, C. Remy, M. Jekel, K.G. Linden, J.E. Drewes, U. Hübner, Evaluation of advanced oxidation processes for water and wastewater treatment – A critical review, Water Res. 139 (2018) 118–131, https://doi.org/10.1016/j.watres.2018.03.042.
[16] N.D.O. Dos Santos, R. Busquets, L.C. Campos, Insights into the removal of microplastics and microfibres by Advanced Oxidation Processes, Sci. Total Environ. 861 (2023), 160665, https://doi.org/10.1016/j.scitotenv.2022.160665.
[17] T. Easton, V. Koutsos, E. Chatzisymeon, Removal of polyester fibre microplastics from wastewater using a UV/H_2O_2 oxidation process, J. Environ. Chem. Eng. 11 (2023), 109057, https://doi.org/10.1016/j.jece.2022.109057.
[18] S. Kim, A. Sin, H. Nam, Y. Park, H. Lee, C. Han, Advanced oxidation processes for microplastics degradation: A recent trend, Chem. Eng. J. Adv. 9 (2022), 100213, https://doi.org/10.1016/j.ceja.2021.100213.
[19] M. Shen, B. Song, C. Zhou, T. Hu, G. Zeng, Y. Zhang, Advanced oxidation processes for the elimination of microplastics from aqueous systems: Assessment of efficiency, perspectives and limitations, Sci. Total Environ. 842 (2022), 156723, https://doi.org/10.1016/j.scitotenv.2022.156723.
[20] Y. Jeong, G. Gong, H.-J. Lee, J. Seong, S.W. Hong, C. Lee, Transformation of microplastics by oxidative water and wastewater treatment processes: A critical review, J. Hazard. Mater. 443 (2023), 130313, https://doi.org/10.1016/j.jhazmat.2022.130313.
[21] M. Feilizadeh, M.R. Karimi Estahbanati, Z. Nayernia, S. Avazpour, P. Drogui, R. D. Tyagi, Chemical degradation of microplastics and nanoplastics in water and wastewater. Current Developments in Biotechnology and Bioengineering, Elsevier,, 2023, pp. 315–332, https://doi.org/10.1016/B978-0-323-99908-3.00014-2.
[22] T.S. Tofa, K.L. Kunjali, S. Paul, J. Dutta, Visible light photocatalytic degradation of microplastic residues with zinc oxide nanorods, Environ. Chem. Lett. 17 (2019) 1341–1346, https://doi.org/10.1007/s10311-019-00859-z.
[23] T.S. Tofa, F. Ye, K.L. Kunjali, J. Dutta, Enhanced visible light photodegradation of microplastic fragments with plasmonic platinum/zinc oxide nanorod photocatalysts, Catalysts 9 (2019) 819, https://doi.org/10.3390/catal9100819.
[24] N. Razali, W.R. Wan Abdullah, N. Mohd Zikir, Effect of thermo-photocatalytic process using zinc oxide on degradation of macro/micro-plastic in aqueous environment, J. Sustain. Sci. Manag. 15 (2020) 1–14, https://doi.org/10.46754/jssm.2020.08.001 [25] L.P.
[25] L.P. Domínguez-Jaimes, E.I. Cedillo-González, E. Luévano-Hipólito, J.D. Acuña-Bedoya, J.M. Hernández-López, Degradation of primary nanoplastics by photocatalysis using different anodized TiO_2 structures, J. Hazard. Mater. 413 (2021), 125452, https://doi.org/10.1016/j.jhazmat.2021.125452.
[26] P.H. Allé, P. Garcia-Muñoz, K. Adouby, N. Keller, D. Robert, Efficient photocatalytic mineralization of polymethylmethacrylate and polystyrene nanoplastics by TiO_2/β-SiC alveolar foams, Environ. Chem. Lett. 19 (2021) 1803–1808, https://doi.org/10.1007/s10311-020-01099-2.
[27] J.D. Acuña-Bedoya, E. Luévano-Hipólito, E.I. Cedillo-González, L.P. Domínguez-Jaimes, A.M. Hurtado, J.M. Hernández-López, Boosting visible-light photocatalytic degradation of polystyrene nanoplastics with immobilized Cu_xO obtained by anodization, J. Environ. Chem. Eng. 9 (2021), 106208, https://doi.org/10.1016/j.jece.2021.106208.
[28] J. Kang, L. Zhou, X. Duan, H. Sun, Z. Ao, S. Wang, Degradation of cosmetic microplastics via functionalized carbon nanosprings, Matter 1 (2019) 745–758, https://doi.org/10.1016/j.matt.2019.06.004.
[29] Y. Cai, F. Chen, L. Yang, L. Deng, Z. Shi, Degradation of Polystyrene Nanoplastics in UV/NaClO and UV/PMS Systems: Insights into Degradation Efficiency, Mechanism, and Toxicity Evaluation, Water 15 (2023) 1920, https://doi.org/10.3390/w15101920.
[30] R. Jiang, G. Lu, Z. Yan, J. Liu, D. Wu, Y. Wang, Microplastic degradation by hydroxy-rich bismuth oxychloride, J. Hazard. Mater. 405 (2021), 124247, https://doi.org/10.1016/j.jhazmat.2020.124247.
[31] V. Piazza, A. Uheida, C. Gambardella, F. Garaventa, M. Faimali, J. Dutta, Ecosafety Screening of Photo-Fenton Process for the Degradation of Microplastics in Water, Front. Mar. Sci. 8 (2022), 791431, https://doi.org/10.3389/fmars.2021.791431.
[32] E. Marcelino-Perez, M. Bonet-Aracil, E. Bou-Belda, A. Amat Payá, A. Arques Sanz, R. Vicente, Polyamide 6.6 Degradation through Photo-Fenton Process, Mater. Sci. Forum 1063 (2022) 243–252, https://doi.org/10.4028/p-28e9b7.

[33] H.-M. Feng, J.-C. Zheng, N.-Y. Lei, L. Yu, K.H.-K. Kong, H.-Q. Yu, T.-C. Lau, M.H. W. Lam, Photoassisted Fenton Degradation of Polystyrene, Environ. Sci. Technol. 45 (2011) 744–750, https://doi.org/10.1021/es102182g.
[34] F. Miao, Y. Liu, M. Gao, X. Yu, P. Xiao, M. Wang, S. Wang, X. Wang, Degradation of polyvinyl chloride microplastics via an electro-Fenton-like system with a TiO_2/graphite cathode, J. Hazard. Mater. 399 (2020), 123023, https://doi.org/10.1016/j.jhazmat.2020.123023.
[35] D. Ortiz, M. Munoz, J. Nieto-Sandoval, C. Romera-Castillo, Z.M. de Pedro, J. A. Casas, Insights into the degradation of microplastics by Fenton oxidation: From surface modification to mineralization, Chemosphere 309 (2022), 136809, https://doi.org/10.1016/j.chemosphere.2022.136809.
[36] K. Hu, P. Zhou, Y. Yang, T. Hall, G. Nie, Y. Yao, X. Duan, S. Wang, Degradation of microplastics by a thermal fenton reaction, ACS EST Eng. 2 (2022) 110–120, https://doi.org/10.1021/acsestengg.1c00323.
[37] D. Amelia, E. Fathul Karamah, M. Mahardika, E. Syafri, S. Mavinkere Rangappa, S. Siengchin, M. Asrofi, Effect of advanced oxidation process for chemical structure changes of polyethylene microplastics, Mater. Today.: Proc. 52 (2022) 2501–2504, https://doi.org/10.1016/j.matpr.2021.10.438.
[38] H. Luo, Y. Zeng, Y. Zhao, Y. Xiang, Y. Li, X. Pan, Effects of advanced oxidation processes on leachates and properties of microplastics, J. Hazard. Mater. 413 (2021), 125342, https://doi.org/10.1016/j.jhazmat.2021.125342.
[39] J. Carbajo, J.E. Silveira, G. Pliego, J.A. Zazo, J.A. Casas, Increasing Photo-Fenton process Efficiency: The effect of high temperatures, Sep. Purif. Technol. 271 (2021), 118876, https://doi.org/10.1016/j.seppur.2021.118876.
[40] J.J. Pignatello, E. Oliveros, A. MacKay, Advanced oxidation processes for organic contaminant destruction based on the Fenton reaction and related chemistry, Crit. Rev. Environ. Sci. Technol. 36 (2006) 1–84, https://doi.org/10.1080/10643380500326564.
[41] M. Tokumura, R. Morito, R. Hatayama, Y. Kawase, Iron redox cycling in hydroxyl radical generation during the photo-Fenton oxidative degradation: Dynamic change of hydroxyl radical concentration, Appl. Catal. B: Environ. 106 (2011) 565–576, https://doi.org/10.1016/j.apcatb.2011.06.017.
[42] Y. Baba, T. Yatagai, T. Harada, Y. Kawase, Hydroxyl radical generation in the photo-Fenton process: Effects of carboxylic acids on iron redox cycling, Chem. Eng. J. 277 (2015) 229–241, https://doi.org/10.1016/j.cej.2015.04.103.
[43] S. Hwang, S.G. Huling, S. Ko, Fenton-like degradation of MTBE: Effects of iron counter anion and radical scavengers, Chemosphere 78 (2010) 563–568, https://doi.org/10.1016/j.chemosphere.2009.11.005.
[44] Y. Ahmed, J. Zhong, Z. Yuan, J. Guo, Roles of reactive oxygen species in antibiotic resistant bacteria inactivation and micropollutant degradation in Fenton and photo-Fenton processes, J. Hazard. Mater. 430 (2022), 128408, https://doi.org/10.1016/j.jhazmat.2022.128408.
[45] G.M. Eisenberg, Colorimetric determination of hydrogen peroxide, Ind. Eng. Chem. Res. 15 (1943) 327–328, https://doi.org/10.1021/i560117a011.
[46] E.B. Sandell, Colorimetric Determination of Traces of Metals, Interscience Pubs.,, New York, 1959, https://doi.org/10.1021/j150441a012.
[47] E. Yousif, R. Haddad, Photodegradation and photostabilization of polymers, especially polystyrene: review, SpringerPlus 2 (2013), 398, https://doi.org/10.1186/2193-1801-2-398.
[48] W. Chu, C.Y. Kwan, K.H. Chan, C.W. Wu, Comprehensive study of the wavelength effect on oxidation processes of 2-chloroaniline, Ind. Eng. Chem. Res. 45 (2006) 3769–3775, https://doi.org/10.1021/ie060141v.
[49] N.M. Ainali, D.N. Bikiaris, D.A. Lambropoulou, Aging effects on low- and high-density polyethylene, polypropylene and polystyrene under UV irradiation: An insight into decomposition mechanism by Py-GC/MS for microplastic analysis, J. Anal. Appl. Pyrolysis 158 (2021), 105207, https://doi.org/10.1016/j.jaap.2021.105207.
[50] L. Tian, Q. Chen, W. Jiang, L. Wang, H. Xie, N. Kalogerakis, Y. Ma, R. Ji, A carbon-14 radiotracer-based study on the phototransformation of polystyrene nanoplastics in water versus in air, Environ. Sci.: Nano 6 (2019) 2907–2917, https://doi.org/10.1039/C9EN00662A.
[51] R. Cao, M.-Q. Zhang, C. Hu, D. Xiao, M. Wang, D. Ma, Catalytic oxidation of polystyrene to aromatic oxygenates over a graphitic carbon nitride catalyst, Nat. Commun. 13 (2022), 4809, https://doi.org/10.1038/s41467-022-32510-x.
[52] A. Bianco, F. Sordello, M. Ehn, D. Vione, M. Passananti, Degradation of nanoplastics in the environment: Reactivity and impact on atmospheric and surface waters, Sci. Total Environ. 742 (2020), 140413, https://doi.org/10.1016/j.scitotenv.2020.140413.
[53] P. García-Muñoz, P.H. Allé, C. Bertoloni, A. Torres, M.U. De La Orden, J. M. Urreaga, M.-A. Dziurla, F. Fresno, D. Robert, N. Keller, Photocatalytic degradation of polystyrene nanoplastics in water. A methodological study, J. Environ. Chem. Eng. 10 (2022), 108195, https://doi.org/10.1016/j.jece.2022.108195.
[54] E. Chamarro, A. Marco, S. Esplugas, Use of fenton reagent to improve organic chemical biodegradability, Water Res. 35 (2001) 1047–1051, https://doi.org/10.1016/S0043-1354(00)00342-0.
[55] M. Hartmann, S. Kullmann, H. Keller, Wastewater treatment with heterogeneous Fenton-type catalysts based on porous materials, J. Mater. Chem. 20 (2010) 9002, https://doi.org/10.1039/c0jm00577k.
[56] R. Pérez-Reverón, J. González-Sálamo, C. Hernández-Sánchez, M. González-Pleiter, J. Hernández-Borges, F.J. Díaz-Peña, Recycled wastewater as a potential source of microplastics in irrigated soils from an arid-insular territory (Fuerteventura, Spain), Sci. Total Environ. 817 (2022), 152830, https://doi.org/10.1016/j.scitotenv.2021.152830.
[57] I. Oller, S. Malato, Photo-Fenton applied to the removal of pharmaceutical and other pollutants of emerging concern, Curr. Opin. Green. Sustain. Chem. 29 (2021), 100458, https://doi.org/10.1016/j.cogsc.2021.100458.
[58] J.A. Zazo, G. Pliego, S. Blasco, J.A. Casas, J.J. Rodriguez, Intensification of the Fenton Process by Increasing the Temperature, Ind. Eng. Chem. Res. 50 (2011) 866–870, https://doi.org/10.1021/ie101963k.
[59] E. Brillas, S. Garcia-Segura, Benchmarking recent advances and innovative technology approaches of Fenton, photo-Fenton, electro-Fenton, and related processes: A review on the relevance of phenol as model molecule, Sep. Purif. Technol. 237 (2020), 116337, https://doi.org/10.1016/j.seppur.2019.116337.